Chiral spontaneous emission propagation based on a honeycomb photonic crystal slab

Zhiyuan Qian,[1] Xuefan Yin,[1] Xinyi Zhou,[1] Feifan Wang,[1] Ye Chen,[1] and Chao Peng[1,2,*]

[1]*State Key Laboratory of Advanced Optical Communication Systems and Networks, Department of Electronics & Frontiers Science Center for Nano-optoelectronics, Peking University, Beijing 100871, China*

[2]*Peng Cheng Laboratory, Shenzhen 518055, China*

(Received 30 December 2023; revised 8 May 2024; accepted 17 May 2024; published 3 June 2024)

We propose the direction-tunable chiral photonic propagation of spontaneous emission based on magnetic helicity and finite-size effect in a topological honeycomb photonic crystal slab. The chiral edge state channels are excited by emitters with magnetic polarization due to the C_6 symmetry, where their propagation directions are tuned by the emitter's position on the magnetic helicity pattern. Meanwhile, the finite size of the honeycomb photonic crystal brings chirality oscillation, which also decides the chirality of photonic propagation. This method of controlling chiral transport in two-dimensional designs can be extended to a three-dimensional silicon-based photonic crystal slab containing a silver split ring resonator as the emitter providing spontaneous emission, which is convenient to fabricate via existing nanotechnology. Moreover, we show the magnetic Purcell effect with chiral transport in the three-dimensional topological PC slab structure. Our research reduces the threshold of on-chip photonic transmission under topological protection, which is helpful for single-photon sources, photonic integrated chip manufacturing, and quantum information processing.

DOI: 10.1103/PhysRevA.109.063504

I. INTRODUCTION

Chiral light transport is one of the essential characteristics of topological photonic structures, which has been performed on a variety of platforms, such as magnetic photonic crystals (PCs) [1–3], coupled-resonator optical waveguides [4–6], and valley photonic structures [7–10]. Transporting inside the structures is more suitable for integrating the topological photon channels on chips than at the interfaces, which leads to the demands based on pseudospin designs, especially honeycomb lattices with C_6 symmetry [11–15]. By controlling the intercell and intracell interaction of C_6 lattices, the interface between the two semi-infinite two-dimensional (2D) honeycomb PCs supporting pseudospin up and down states, respectively, works as the photon channel [11,16–18]. The chiral propagation excited by sources with magnetic spin formation provides photonic guidance following the slope of edge state bands, which determines the directions of the photonic stream [11,18–20]. However, when constructing a specific structure, the band-based direction judgment from reciprocal space must be more intuitive and often restricted by structural changes in the simulations and experiments. New direction judgments based on the real-space mode distribution are required for practical fabrication, which is convenient to control the chiral channels working in the desired way. Meanwhile, it might be intuitively assumed that the bulk band theory of infinite periodic PCs determines chiral propagation in finite-size PCs. The influence of the finite-size effect on chiral transport may not be overlooked.

So far, researchers have widely explored the nature of topological photonics and proposed many experiments in which the bulk band theory of infinite periodic PCs determines chiral propagation in finite-size PCs [3,21–27] to approach the motivation of realizing controlled and highly efficient photon transmission on-chip and boosting quantum manipulation [4,13,28–32], but there is still a considerable distance to go. For example, topological states based on some 2D photonic structures, especially honeycomb lattices, only exist in transverse magnetic-like (TM-like) modes with H_x, H_y, and E_z [11,14,33,34], which requires perfect electric conductors such as metallic plates at the top and bottom interfaces of the PC slabs to eliminate the transverse electric-like (TE-like) modes with E_x, E_y, and H_z. However, when considering on-chip photonic integrating, there is still trouble in fabricating metallic plates together with dielectric lattices in the three-dimensional (3D) slab for existing processing micro- and nanotechnologies such as deposition, electron-beam lithography (EBL), and inductively coupled plasma (ICP) etching [35–39]. Meanwhile, as the current usual chiral emitters, quantum dots need low temperatures and a strong magnetic field [13]. These difficulties limit the practical applications of on-chip topological chiral photonic channels.

In this work, we propose the direction-tunable chiral photonic propagation of spontaneous emission based on the magnetic helicity and finite-size effect in a topological honeycomb PC slab matching the present manufacturing of on-chip photonic integrating. We reveal the principle of chiral transport depending on the emitter's position inside the PC upon the magnetic helicity distribution of TM modes, acting as a new real-space judgment of chiral directions in 2D simulation. More importantly, we found a phenomenon of "chirality oscillation" caused by the finite-size effect in the frequency range

*pengchao@pku.edu.cn

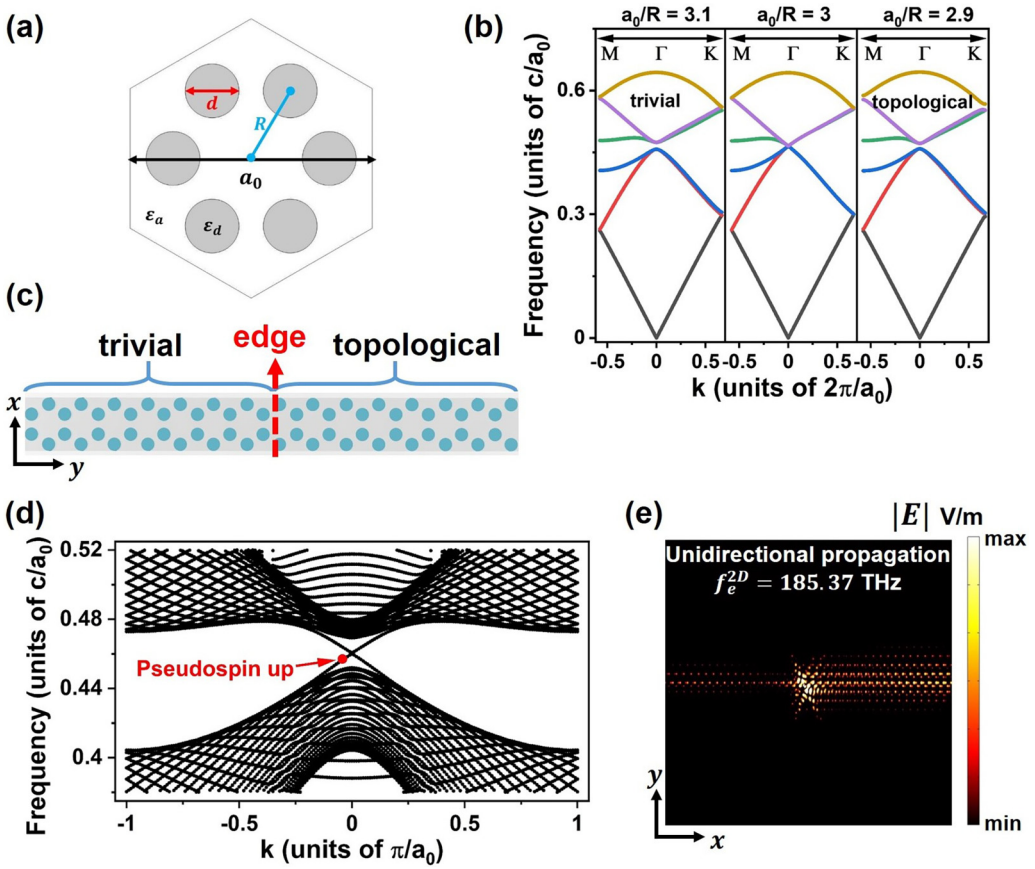

FIG. 1. (a) Schematic diagram of the single hexagon artificial cell composed of six cylinders as the building block of the 2D honeycomb photonic lattices. (b) The band-gap structures of C_6 lattices in (a) with different a_0/R. (c) Schematic diagram of the 2D supercell structure, which is periodic in the x direction, and of ten artificial cells for both topological ($a_0/R = 2.9$) and trivial ($a_0/R = 3.1$) regions in the y direction. (d) The projected band-gap structure of supercell in (c) showing the two edge state bands corresponding to pseudospin up and down states from C_6 symmetry. (e) The electric field distribution for unidirectional propagation excited by a chiral emitter through the edge state channel giving the eigenfrequency $f_e^{2D} = 185.37$ THz.

of edge state channels, which also influences the photonic chiral propagation. The tunable chiral modes based on these principles in the 2D structures can be extended to modes in a 3D topological PC slab with SiO_2-PC-SiO_2 sandwich structures. By careful design, the 3D slab structure is convenient for fabricating via existing nanotechnology, including deposition, EBL, and ICP etching. A silver split ring resonator (SRR) can be utilized as the chiral emitter instead of quantum dots so that the entire system can work at room temperature. Moreover, we show the tunable magnetic Purcell enhancement excited by SRR combined with chiral transport in the 3D topological PC slab structure. Our research reduces the threshold of on-chip chiral photonic application under topological protection, which is helpful for single-photon sources, photonic integrated chip manufacturing, and quantum information processing.

II. 2D MODULE OF HONEYCOMB PHOTONIC CRYSTAL SETUP

The 2D honeycomb photonic lattices are triangularly paved with hexagon artificial cells composed of six cylinders [Fig. 1(a)]. Considering the harmonic TM modes of electromagnetic wave, namely, the modes with out-of-plane E_z and in-plane H_x and H_y, a pseudo-time-reversal symmetry can be obtained by the two 2D irreducible representations of the C_6 symmetry group from artificial cells' geometry, which leads to the two pseudospin states corresponding to positive and negative angular momenta of E_z [11].

The intercell and intracell interaction of C_6 lattices determine the photonic topological property, which can be quantified by a_0/R, where a_0 donates lattice constant and R represents the distance between cylinders and the cell center. The cylinders of artificial cells are set as silicon in the working wavelength with permittivity $\varepsilon_d = 12$ and diameter $d = 2a_0/9$, while the other space is filled with silica $\varepsilon_a = 2$. The band-gap structures varying with a_0/R are given in Fig. 1(b). The balance of intercell and intracell interaction of C_6 lattices is at $a_0/R = 3$, where the Dirac point appears at the Γ point. When the lattices shrink to $a_0/R = 3.1$, the intracell interaction holds the dominant position, and the photonic band gap is open, leading to the topological trivial structure. While the lattices expand to $a_0/R = 2.9$, the intercell interaction dominates the lattices, and the band gap reopens near the Dirac point with a band inversion, which means the topological property changes.

The honeycomb topological photonic waveguide structure comprises two 2D C_6 PCs with different a_0/R and

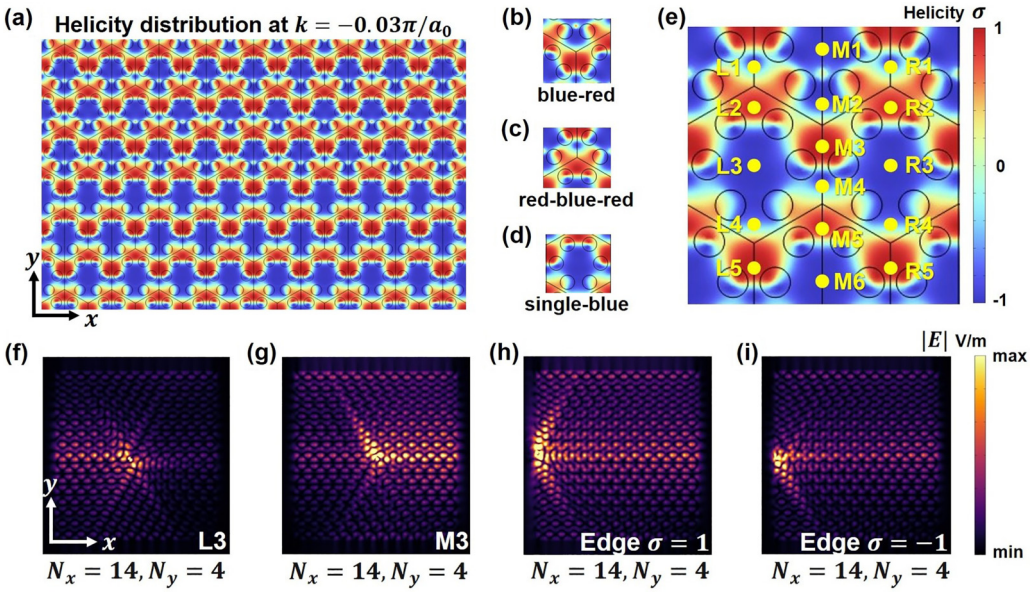

FIG. 2. Chiral photonic propagation determined by magnetic helicity. (a) The magnetic helicity pattern for the pseudospin up states from the positive-slope band branch at $k = -0.03\pi/a_0$, consisting of (b) blue-red, (c) red-blue-red, and (d) single-blue types of lattice elements distinguished by the central colors that red represents $\sigma \to 1$ while blue means $\sigma \to -1$. (e) The positions of emitters marked by L1–L5, M1–M6, and R1–R5 corresponding to (b)–(d) around the interface of the two 2D honeycomb PCs. The (f) left and (g) right chiral propagation in the areas of $\sigma = -1$ and $\sigma = 1$, respectively. The (h) right and (i) left chiral propagation excited by the emitter near the edge of the entire PC structure in the areas of $\sigma = 1$ and $\sigma = -1$, respectively. The size of (f)–(i) is $N_x = 14$, $N_y = 4$. The emitter takes the form of $(1, i, 0)$ with the frequency $f_e^{2D} = 185.37$ THz.

topological properties. Here, we use the supercell structure shown in Fig. 1(c) for simulation with $a_0 = 740$ nm, which is periodic in the x direction and of ten artificial cells for both topological ($a_0/R = 2.9$) and trivial ($a_0/R = 3.1$) regions in the y direction. The band gap is given in Fig. 1(d) with clearly two edge state bands corresponding to pseudospin up and down states from C_6 symmetry. The band with a positive slope represents the pseudospin up state, while the negative slope means the pseudospin down state. These bands of edge states lead to the available photonic channels under topological protection; for example, Fig. 1(e) shows the electric field distribution for unidirectional propagation excited by a chiral emitter through the edge state channel with the eigenfrequency $f_e^{2D} = 185.37$ THz. Moreover, the positive and negative slope of edge state bands originating from pseudospin up and down states imply that this topological photonic channel supports chiral light transport.

III. CHIRAL PHOTONIC PROPAGATION DETERMINED BY MAGNETIC HELICITY PATTERNS

According to the band theory of infinite periodic PCs, the chiral direction strictly obeys the slope of edge state bands. However, the band-based judgment from reciprocal space is not intuitive enough to construct a specific topological waveguide due to the lack of the emitter's position information. Here, we propose the direction-tunable chiral spontaneous emission based on the magnetic helicity, a method containing position information based on real-space mode distribution, which is convenient for controlling the chiral channels working in the desired way. It is worth noting that magnetic helicity is a generalization from the band theory, which avoids the influence of finite size. Therefore, the PC size should be unchanged when exploring the chiral transport for different emitter positions in the practical situation. The magnetic helicity, similar to its electric version [40,41], can be defined as

$$\sigma_z = \frac{2 \times \mathrm{Im}(H_x H_y^*)}{|H_x|^2 + |H_y|^2}; \tag{1a}$$

$$\sigma_x = \frac{2 \times \mathrm{Im}(H_y H_z^*)}{|H_y|^2 + |H_z|^2}; \tag{1b}$$

$$\sigma_y = \frac{2 \times \mathrm{Im}(H_z H_x^*)}{|H_z|^2 + |H_x|^2}. \tag{1c}$$

Considering the TM modes in the 2D situation, $H_z \equiv 0$, leading to $\sigma_x = \sigma_y = 0$, thus only σ_z should be concerned. The total magnetic helicity $\sigma = \sigma_z \in [-1, 1]$.

Based on the supercell shown in Fig. 1(c), we can obtain the distribution of magnetic helicity via electromagnetic modes. For the pseudospin up states from the positive-slope band branch, the magnetic helicity pattern is shown as Fig. 2(a) at $k = -0.03\pi/a_0$ corresponding to the red point in Fig. 1(d), where red represents helicity $\sigma \to 1$ while blue means $\sigma \to -1$. The helicity patterns are almost the same for other values of k from the positive-slope band branch. In contrast, for the pseudospin down states from the negative-slope branch, the signatures of helicity are all opposite. Here, we take the pseudospin up states at $k = -0.03\pi/a_0$ as an example. The pattern comprises three types of lattice elements, distinguished by the central colors, i.e., blue-red, red-blue-red, and single-blue types, as shown in Figs. 2(b), 2(c), and 2(d), respectively. These three types all consist of red and blue areas, i.e., $\sigma \to \pm 1$.

The helicity pattern functions as a map for emitters to obtain chiral direction. To excite the edge states, the emitters of spontaneous emission must have the form of magnetic spin, namely, $S_{\pm} \sim H_0(\hat{x} \mp i\hat{y})$. We use the emitters with the left and right magnetic spin forms $(1, \pm i, 0)$ to excite the chiral modes. Sixteen points are chosen to place the emitters corresponding to the three types of lattice elements, marked by L1–L5, M1–M6, and R1–R5, around the interface of the two 2D honeycomb PCs [Fig. 2(e)]; it is clear that points L4, L5, M2, M3, R4, and R5 correspond to the up and down positions of the blue-red type [Fig. 2(b)]; points L1, L2, M4, M5, R1, and R2 correspond to the up and down positions of the red-blue-red type [Fig. 2(c)], points L3, M1, M6, and R3 correspond to the center positions of the single-blue type [Fig. 2(d)]. Then, finite-element simulations are performed using commercial COMSOL MULTIPHYSICS software, which can simulate optical modes and photon propagation for various photonic structures [29,42–44]. The entire model is surrounded by the perfect-matched-layer (PML) boundary condition. During the investigation of chiral transport for different emitter positions, the PC size should be fixed. When the fixed x-directional period of PCs is not too large, i.e., $N_x < 30$ in our simulation, by collecting all results of light propagation excited by the emitter with the spin form $(1, i, 0)$ and frequency $f_e^{2D} = 185.37$ THz with different emitter's positions, we find that when the emitter is placed in the area of helicity $\sigma = -1$ marked in blue, including the positions L1, L3, L4, M1, M2, M4, M6, R1, R3, and R4, the photons are guided to the left side [Fig. 2(f)], while the photons turn to the right side [Fig. 2(g)] with the emitter in the area of $\sigma = 1$ marked in red, including the points L2, L5, M3, M5, R2, and R5. The directionality of chiral propagation is robust in that it cannot be broken by impurities and waveguide bents, which has been proven in plenty of research [12–14,22]. Moreover, the chiral direction remains when emitters are placed near the edge of the entire module. As shown in Fig. 2(h), the emitter in the area of $\sigma = 1$ excites the propagation of the right direction, while moving the emitter to $\sigma = -1$, the light propagation is partly eliminated because the PML boundary absorbs photons in the left direction [Fig. 2(i)]. Also, when the emitter takes the other spin form $(1, -i, 0)$, the situations of chiral photon propagation are opposite. We point out that during the discussion of tuning chiral transport by the emitter's position, the PC size and emitter frequency should be unchanged. The influence of the finite-size effect is elaborated in Sec. IV.

IV. CHIRAL PHOTONIC PROPAGATION DETERMINED BY FINITE SIZE

The finite-size effect cannot be well explained by the bulk band theory of infinite periodic PCs. The method of magnetic helicity distribution we propose in Sec. III is a generalization from the band theory with additional position information, which cannot fully address this problem. Instead, we consider a finite-size PC, in which a length L in the x direction gives rise to discrete wave vectors with $\delta k = \pi/L$ and discrete eigenfrequencies accordingly. As shown in Fig. 3(a), these discrete eigenfrequencies can be marked as $f_1, f_2, \ldots, f_n$, and for $f < f_1$ or $f > f_n$, the bulk modes will interfere with the edge state channel. A similar effect has been discussed in the context of miniaturized bound states in the continuum (BICs) in the theory [45] and experiments [38]. We present a simplified analytic model to depict the finite-size effect in honeycomb topological PCs (Appendix A). Then, we reveal a phenomenon denoted as "chirality oscillation," which can be understood from the interaction between the left and right chiral modes at the finite size boundary, similar to the hybridization of chiral edge states in Su-Schrieffer-Heeger (SSH) models [46].

The discrete eigenfrequencies in finite-size PCs can be solved by numerical simulation (COMSOL MULTIPHYSICS). We take the size $N_x = 30, N_y = 10$ as an example. In the frequency range of edge states, this finite-size PC gives eigenfrequencies $f_e^{2D} = f_1, f_2, \ldots, f_6$, shown in Fig. 3(b), which belongs to a series of edge states but folded by finite size. Note that these solutions are not pseudospin states and show no chirality, confirmed by the results of the electromagnetic field excited by a chiral emitter.

We fix the emitter at an unchanged position for fair comparison. In particular, we take the emitter as $(1, i, 0)$ at point L3 as an example. The eigenfrequency points divide the frequency range of the edge state into several intervals, where the chiral emitter can excite light transporting with different chirality, showing as chirality oscillation [Fig. 3].

To quantitatively determine the direction of chiral propagation, we define the parameter

$$C_{ln} = \ln \frac{\int E_{\text{left}} dS}{\int E_{\text{right}} dS}. \tag{2}$$

$C_{ln} > 0$ means left propagation, and $C_{ln} < 0$ means right propagation. We choose the two left and right zones with the same area S near the interface between the two honeycomb PCs, and integrate the electromagnetic field. Note that when $f < f_1 = 182.78$ THz or $f > f_6 = 188.96$ THz, bulk modes will interfere with the edge state channels. The zero points of C_{ln} are also the eigenfrequency points $f_1 \sim f_6$. It is readily found that the chirality in one interval separated by two eigenfrequency points is opposite to its neighbor two intervals. The whole curve of C_{ln} shows the chirality oscillation.

The chiral direction of one interval is determined by the parity of the two eigenmodes at the beginning and end points of the interval. The parity here refers to the mirror-x parity about the $x = 0$ axis of the PC. The parity of eigenmodes originates from the finite size, which can be seen in Appendix A. Considering the chiral emitter $(1, i, 0)$ at the fixed L3 point, if the beginning point's eigenmode is odd symmetric and the end point's eigenmode is even, this interval experiences odd to even symmetry, then the chiral direction is left. Otherwise, the chiral direction is right if the interval experiences even to odd symmetry.

The eigenmodes' parity can be seen through the E_z pattern. For example, as shown in Figs. 3(c)–3(e), we identify that the parity of the three neighbor eigenfrequency points $f_2 = 184.08$ THz, $f_3 = 185.35$ THz, and $f_4 = 186.38$ THz is even, odd, and even symmetric, respectively. According to the theory above, the interval (f_2, f_3) supports the right chiral direction, while the interval (f_3, f_4) supports the left one. One can verify the chiral direction by choosing any frequency point that belongs to the intervals, such as the cases

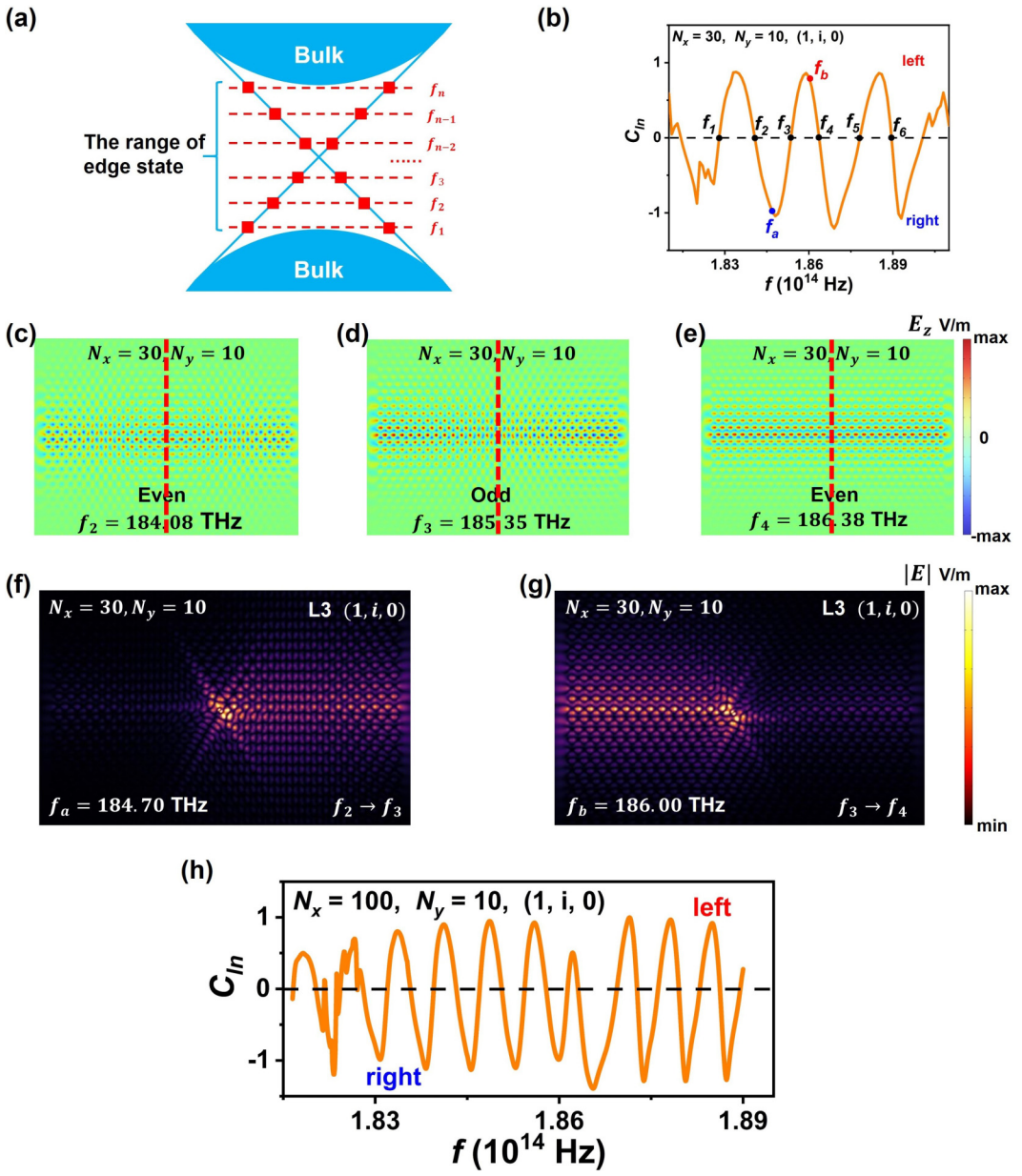

FIG. 3. Chiral photonic propagation determined by finite size. (a) Schematic diagram of the discrete eigenfrequencies dividing the range of edge state into several intervals. (b) Chirality oscillation with finite size $N_x = 30$, $N_y = 10$. $C_{ln} > 0$ means left chiral direction, and $C_{ln} < 0$ means right. The parity of eigenmodes shown by E_z pattern with finite size $N_x = 30$, $N_y = 10$ and different eigenfrequencies (c) $f_2 = 184.08$ THz, (d) $f_3 = 185.35$ THz, and (e) $f_4 = 186.38$ THz, respectively. The parity refers to the mirror-x parity about the $x = 0$ axis of the PC marked in red dash lines in (c)–(e). The chiral transport with finite size $N_x = 30$, $N_y = 10$ and frequencies (f) $f_a = 184.70$ THz and (g) $f_b = 186.00$ THz, respectively. (h) Chirality oscillation with finite size $N_x = 100$, $N_y = 10$. The chiral emitter takes the form of $(1, i, 0)$ at the L3 point.

of $f_a = 184.70$ THz and $f_b = 186.00$ THz shown in Figs. 3(f) and 3(g), respectively.

The chirality dependency on the parity holds for all finite sizes of PC. When comparing $N_x = 30, N_y = 10$ and $N_x = 40, N_y = 10$, they happen to have the same eigenfrequency point $f_1 = 182.78$ THz. However, for $N_x = 30, N_y = 10$, the eigenmode is odd symmetric, while for $N_x = 40, N_y = 10$, the eigenmode is even, so they will give different chiral directions if we choose a frequency point nearby, like $f = 183.00$ THz gives left direction for $N_x = 30, N_y = 10$ while right direction for $N_x = 40, N_y = 10$. Note that the chiral emitter $(1, -i, 0)$ at point L3 or $(1, i, 0)$ at point M3 gets opposite situations.

We note that the phenomenon of chirality oscillation still happens in large sizes, even in the case of $N_x = 100, N_y = 10$ [Fig. 3(h)]. Besides, if the system's loss can be well controlled, the finite-size chirality can still exist, as seen in Appendix B. If $N_x \to \infty$, the interaction between the left and right chiral modes vanishes, then the transport behavior follows the chirality given by the bulk band theory.

From the view of chiral photonic propagation in finite-size PCs, we can explain the chiral inversion by changing finite sizes with emitter $(1, i, 0)$ at point L3, as shown in Figs. 4(a)–4(c), which is just a manifestation of the chirality oscillation. The corresponding chirality oscillation near

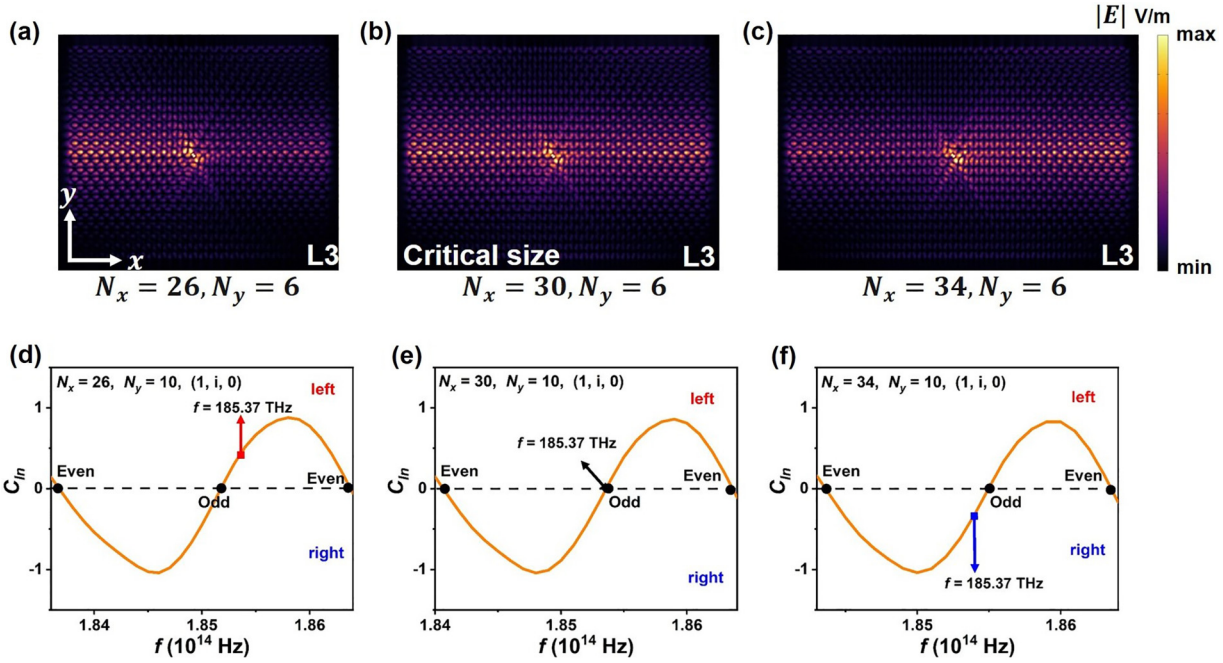

FIG. 4. The chiral inversion as a piece of chirality oscillation. The photonic propagation with the size of (a) $N_x = 26$, $N_y = 6$, (b) $N_x = 30$, $N_y = 6$, and (c) $N_x = 34$, $N_y = 6$. Chirality oscillation with different finite sizes (d) $N_x = 26$, (e) $N_x = 30$, and (f) $N_x = 34$. The emitter at point L3 takes the form of $(1, i, 0)$ with the frequency $f = 185.37$ THz.

$f = 185.37$ THz for $N_x = 26$, $N_x = 30$, and $N_x = 34$ can be shown in Figs. 4(d)–4(f). The change of N_x will slowly move the eigenfrequency. Note that the results are almost unaffected by the y direction for $N_y \geqslant 4$. When fixing the frequency of emitter at $f = 185.37$ THz, it will excite the left chiral direction for $N_x < 30$ shown in Fig. 4(a) because the interval of f experiences odd to even symmetry as shown in Fig. 4(d). Then, the frequency f will cross one of the eigenfrequency points at $N_x = 30$, so we obtain almost no chirality, as shown in Figs. 4(b) and 4(e). When $N_x > 30$, the emitter's frequency gets into another interval with opposite chirality, so the emitter $(1, i, 0)$ excites the right directional transport, as shown in Figs. 4(c) and 4(f). Therefore, the change of chirality determined by finite size can be explained.

Within each chiral interval, the method of tuning chiral direction by the emitter's position in Sec. III is still valid. For example, one can choose an emitter with any chirality and a given frequency, putting it into any position in the given PC structure to test the chiral direction. Then, one can predict the chiral direction of any emitter by using the helicity pattern map. In other words, both the magnetic helicity pattern and the finite size of topological PCs control the chiral direction.

In summary of the finite-size effect, we found the phenomenon of chirality oscillation in the frequency range of edge states caused by the hybridization of edge states in honeycomb topological PCs. The finite-size effect gives rise to discrete eigenfrequency points with no chirality, which divides the spectrum into several intervals with different chirality from their neighbor intervals, showing the chirality oscillation. As a result, the chirality in each interval depends on the chiral emitter and the parity of the two eigenmodes at the ending points of the interval. Such a complex behavior of chiral propagation indeed cannot be explained from bulk band theory.

V. CHIRAL PROPAGATION BASED ON HONEYCOMB PHOTONIC CRYSTAL SLAB

For experimental and practical applications, the proposal of 2D tunable chiral photonic guiding modes based on magnetic helicity and finite size should be extended to its 3D version, which is limited by the present ability of microfabrication. The 2D tunable chiral photonic waveguides designed in three dimensions are TM-like modes with H_x, H_y, and E_z, which requires perfect electric conductors to eliminate the TE-like electromagnetic components, i.e., E_x, E_y, and H_z. In the previous research [11,14,33,34], metallic plates covered at the interfaces of PCs can play a role in keeping TM-like electromagnetic fields; nevertheless, they can only be utilized in some small-scale demonstration experiments. When considering on-chip photonic integration, it is hard to fabricate large bulk metal covering dielectric lattices in the 3D slab for existing processing nanotechnology.

An available way is to construct the 3D topological PC slab structures in TM-like modes hybrid with H_z components due to the finite size in the z direction, similar to the works of couple-wave theory for photonic crystal surface-emitting lasers [47–50] and bound states in the continuum [38,51,52]. In our work, we construct the 3D honeycomb topological waveguide slab with SiO_2-PC-SiO_2 sandwich structures based on the results of the 2D chiral photonic guiding modes from magnetic helicity and finite size [Fig. 5(a)]. Note that the chiral emitter in the 3D module should be a physical entity, which is a silver SRR in our design. The SRR can be excited either endogenously or exogenously for the photonic chip. Also, because of the tiny size contrast to the PC structure, the SRR can still be treated as a point when focusing on the chiral light transport. Since the 3D topological PC slab is extended by 2D structure, it inherits all the parameters of 2D cases, like

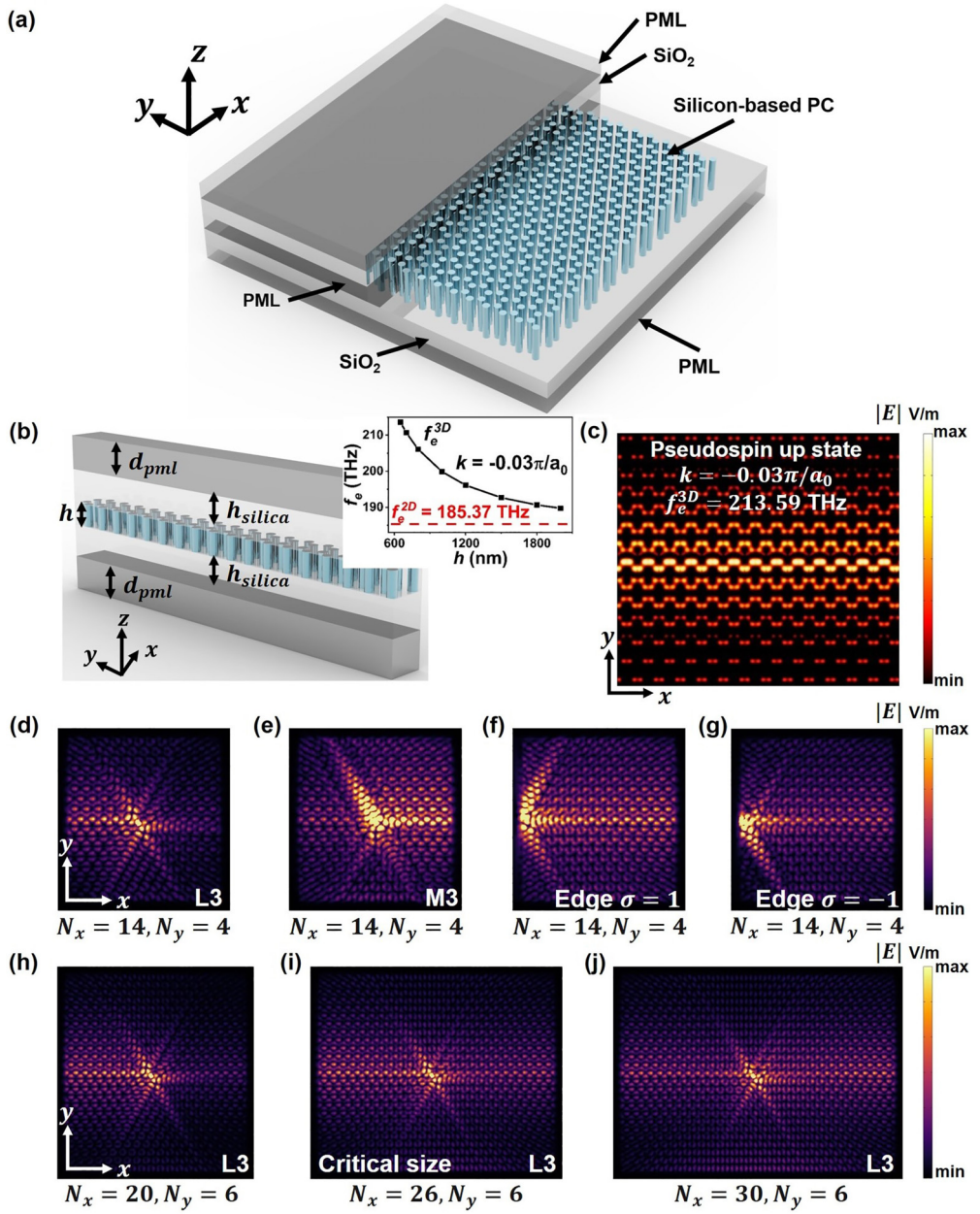

FIG. 5. Chiral propagation based on honeycomb photonic crystal slab. (a) Schematic diagram of the 3D honeycomb topological SiO_2-PC-SiO_2 sandwich slab structure with the PC layer's thickness $h = 650$ nm and silica layers' thickness $h_{\text{silica}} = 1403.6$ nm, surrounded by the PML layers with $d_{\text{pml}} = 701.8$ nm. (b) Schematic diagram of the 3D supercell structure, which is periodic in the x direction, of five artificial cells for both topological ($a_0/R = 2.9$) and trivial ($a_0/R = 3.1$) regions in the y direction, and covered by silica and PML layers at the top and bottom faces in the z direction. The inset in (b) shows the eigenfrequency f_e^{3D} of pseudospin up state at $k = -0.03\pi/a_0$ varying with h. (c) The electric field distribution of pseudospin up edge state at $k = -0.03\pi/a_0$ by the supercell of (b), giving $f_e^{3D} = 213.59$ THz. (d) and (e) The left and right chiral propagation excited by the emitter at points L3 and M3, respectively. (f) and (g) The right and left chiral propagation excited by the emitter near the edge of the entire structure in the areas of $\sigma = 1$ and $\sigma = -1$, respectively. The size of (d)–(g) is $N_x = 14$, $N_y = 4$. (h)–(j) The chiral photonic propagation with the PC size of $N_x = 20$, $N_y = 6$; $N_x = 26$, $N_y = 6$; and $N_x = 30$, $N_y = 6$, respectively.

$a_0 = 740$ nm, $\varepsilon_a = 2$, $\varepsilon_d = 12$, $d = 2a_0/9$, and $a_0/R = 2.9$ for topological regions, and $a_0/R = 3.1$ for trivial regions. Additionally, the SiO_2-PC-SiO_2 sandwich structure is comprised of a PC layer with the thickness $h = 650$ nm and two upper and lower silica layers with $h_{\text{silica}} = \lambda_e^{3D} = c/f_e^{3D} = 1403.6$ nm. Then, the SiO_2-PC-SiO_2 sandwich is surrounded by the PML layers with the thickness $d_{\text{pml}} = \lambda_e^{3D}/2 = 701.8$ nm. The eigenfrequency f_e^{3D} is solved in a 3D supercell structure [Fig. 5(b)], which is periodic in the x direction, of five artificial cells for both topological ($a_0/R = 2.9$) and trivial ($a_0/R = 3.1$) regions in the y direction, and covered by silica and PML layers at the top and bottom faces in the z direction. It is noted that the 3D simulation costs much more time and resources, including cores and memories, than

2D simulation, so it is difficult to obtain the complete 3D band-gap structure like the 2D cases [Fig. 1(d)], but we can solve some particular eigenvalue points based on the results of 2D cases. At $k = -0.03\pi/a_0$ from the positive slope band branch, the eigenfrequency of pseudospin up edge state is $f_e^{3D} = 213.59$ THz in 3D conditions [Fig. 5(c)], which is larger than $f_e^{2D} = 185.37$ THz in 2D situations because of the influence of extra H_z components depending on the PC's thickness h. The larger thickness h leads to smaller f_e^{3D}, and if h is large enough, $f_e^{3D} \to f_e^{2D}$, which can be seen in the inset of Fig. 5(b). For example, when $h = 2000$ nm, we get $f_e^{3D} = 189.75$ THz at $k = -0.03\pi/a_0$, very close to the f_e^{2D}. Also, h cannot be too small; otherwise, it will be hard to find the eigenfrequency due to the disturbances of H_z components. Therefore, it is suitable to set $h = 650$ nm in our simulation.

Then we discuss the chiral propagation using the 3D topological PC waveguide with the size of $N_x = 14, N_y = 4$ by setting the magnetic spin emitter with $f_e^{3D} = 213.59$ THz as the form of $(1, i, 0)$ at the points shown in Fig. 2(e) in the xy plane with z taking the center value $z = 0$. The results of chiral propagation are almost the same as those in 2D conditions: when the finite size of N_x is not too large, the emitter in the areas of $\sigma = -1$ makes photons turn left, while $\sigma = 1$ leads to right-guided photons. For example, the emitter $(1, i, 0)$ at point L3 excites the chiral left propagation [Fig. 5(d)], while at point M3 for right propagation [Fig. 5(e)]. If the emitter is close to the edge of the entire system, the chiral photonic direction shows robustness against the effect of the edge. As shown in Fig. 5(f), the emitter's place of $\sigma = 1$ allows light to turn right, while shown in Fig. 5(g), the $\sigma = -1$ place makes the left propagation absorbed by PML layers, leaving the weaker field distribution similar to those in 2D cases like Fig. 2(i).

The influence of topological PC size should also be considered carefully. It costs plenty of computing resources in the 3D large-size simulation due to the over 10^7 degrees of freedom. Besides the size of $N_x = 14, N_y = 4$ shown in Figs. 5(d)–5(g), we also simulate with the larger size $N_x = 20, N_y = 6$ [Fig. 5(h)], $N_x = 26, N_y = 6$ [Fig. 5(i)], and $N_x = 30, N_y = 6$ [Fig. 5(j)] with the emitter $(1, i, 0)$ at point L3. In the study of 2D cases, we find the direction of chiral photon propagation is affected by the size of the entire PC structure with a critical size of $N_x = 30, N_y = 6$ [Figs. 4(a)–(c)]. Similarly, the simulations of 3D cases give the critical size for 3D conditions near $N_x = 26, N_y = 6$. Comparing the electric field distributions with different sizes [Figs. 5(h)–(j)], besides the major electric parts in the chiral left direction, some minor components exist in the right direction, and get larger with the increment of PC size. When the size increases to $N_x = 30, N_y = 6$, the major photonic channel changes to the right direction. This chirality inversion has been explained in Sec. IV as a piece of chirality oscillation. Therefore, the influence of size in the chiral direction still exists in the 3D situation, which should be taken into consideration in the practical fabrication. Overall, it is meaningful to show that the method of controlling the chiral photon transport based on magnetic helicity σ and finite size N_x still works for a 3D honeycomb topological PC slab, which means people can tune the chiral channels directly with real-space judgment in the fabrication.

VI. DISCUSSION ON PURCELL EFFECT AND EXPERIMENTAL IMPLEMENTATION

Since we propose that we can utilize silver SRR as the chiral emitter, it is necessary to discuss the details of the SRR's function, especially the spontaneous emission enhancement, i.e., the Purcell effect in the topological waveguide. Most studies of the Purcell effect focus on the electric, not magnetic, response because the electric dipole response is always the most powerful in electromagnetic radiation, and the magnetic dipole response will be much weaker. However, the electric Purcell effect systems cannot match the magnetic spin form of the emitter and excite chiral propagation, which requires a magnetic response. So far, the magnetic Purcell effect has been explored in theory [53,54] and realized by metamaterials [55], nanoantennas [56], and nanocavities [57,58]. Here, we take the silver SRR structure [Fig. 6(a)] as the magnetic nanoantenna to achieve an excellent magnetic response, widely used in metamaterials research [59–61].

The resonant frequency of SRR should be the same as the eigenfrequency f_e^{3D}, which we set as 213.59 THz [Fig. 6(b)], so that the size of the silver SRR is $R_{out} = 35$ nm, $R_{in} = 25$ nm, $w = 10$ nm, and $d_c = 27.66$ nm, where w donates the width of the split, d_c is the depth of the ring, and R_{out} and R_{in} represent the outer and inner radius of the ring, respectively, shown in Figs. 6(a) and 6(b). The dielectric constant of silver is taken from the experimental data [62]. We take the same axis orientation as Fig. 5(a). The ring plane of SRR is parallel to the xz plane, and the emitter is placed at the center of the ring, which is also point L3 or M3. The topological PC's size is $N_x = 14, N_y = 4$, so that no chiral oscillation should be considered here.

The Purcell factor of spontaneous emission is defined as $F = \gamma/\gamma_0$ [63], where γ and γ_0 donate the spontaneous emission rate in the systems and vacuum, respectively. In our structure, the total rate γ_{tot} can be divided into several contributions: the absorption part γ_{abs}, the left and right propagation part γ_{left} and γ_{right} by edge state channel, and the scattering part γ_{sc}, i.e., $\gamma_{tot} = \gamma_{abs} + \gamma_{left} + \gamma_{right} + \gamma_{sc}$. For every term, $\gamma_i/\gamma_0 = W_i/W_0 \quad (i = \text{tot, abs, left, right, sc})$, so the simulation of spontaneous emission rate can be turned into the simulation of energy [29,43]. W_{tot} and W_0 are the total emitted energy in the systems and free space, respectively, obtained by surface integrals of a nanosphere enveloping the emitter over the energy flows. W_{abs} is the absorption for the silver SRR as the mathematical form of the volume integrals of energy loss. W_{left} and W_{right} are the energy guided into the chiral left and right edge state channels, respectively, given by the surface integrals of the cross section of the honeycomb PC structures over the energy flows. W_{sc} is the energy dissipation into the far field, given by the surface integrals over energy flows on boundaries without edge state channels.

We first discuss the chiral enhanced spontaneous emission with different split directions. When placing the SRR containing emitter $(1, i, 0)$ at point M3, the chiral propagation turns right [Figs. 6(c) and 6(d)], the same as those without SRR [Fig. 5(e)]. When the split of SRR is in the $+x$ direction, namely, the right direction, the Purcell factors $F_{tot} = 8.64$, $F_{abs} = 5.88$, $F_{left} = 0.13$, $F_{right} = 0.55$, and $F_{sc} = 2.08$, showing that $F_{left}/F_{right} = 1{:}4.10$, brings the chiral right

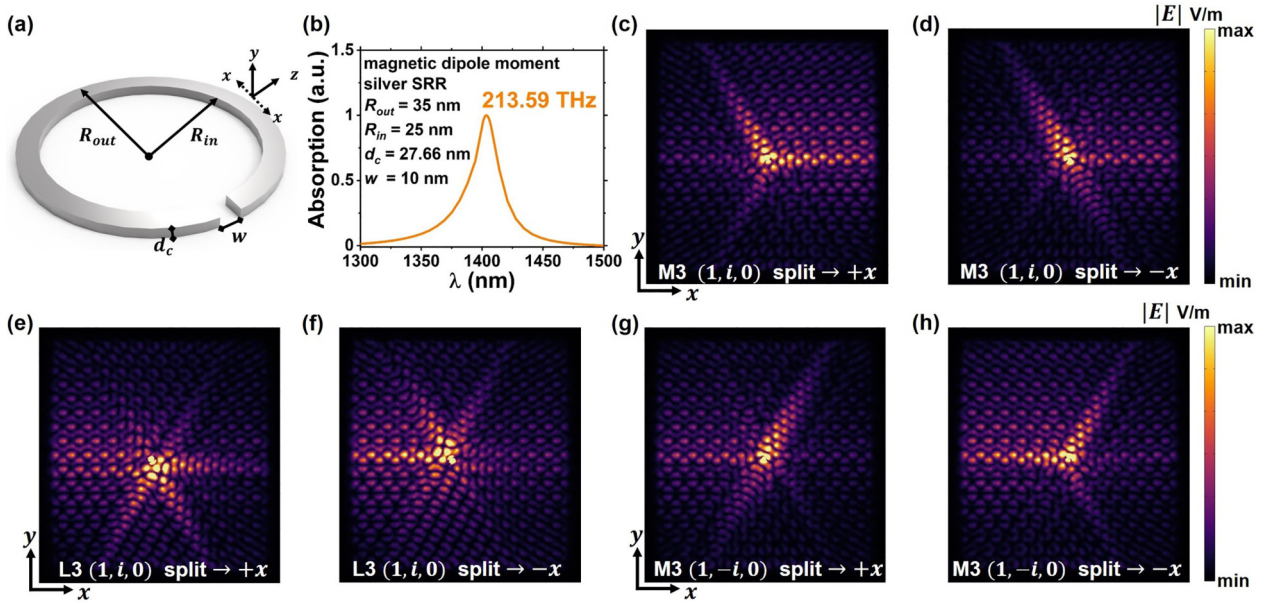

FIG. 6. Magnetic Purcell effect combined with chiral photonic propagation based on honeycomb photonic crystal slab. (a) Schematic diagram of the silver SRR with $R_{\text{out}} = 35$ nm, $R_{\text{in}} = 25$ nm, $w = 10$ nm, and $d_c = 27.66$ nm. (b) The absorption spectrum of the silver SRR in (a) showing the resonant frequency at 213.59 THz. (c)–(h) The chiral Purcell enhancement transport depends on different emitter positions, emitter polarizations, and split directions, which are (c) point M3, $(1, i, 0)$, $+x$ direction, (d) point M3, $(1, i, 0)$, $-x$ direction, (e) point L3, $(1, i, 0)$, $+x$ direction, (f) point L3, $(1, i, 0)$, $-x$ direction, (g) point M3, $(1, -i, 0)$, $+x$ direction, and (h) point M3, $(1, -i, 0)$, $-x$ direction, respectively. The ring plane of SRR is parallel to the xz plane and the emitter is at the center of ring.

photonic propagation [Fig. 6(c)]. Meanwhile, the split of the $-x$ direction, namely, the left direction, leads to the right chiral light transport [Fig. 6(d)], giving the Purcell factors $F_{\text{tot}} = 8.37$, $F_{\text{abs}} = 5.73$, $F_{\text{left}} = 0.08$, $F_{\text{right}} = 0.29$, and $F_{\text{sc}} = 2.27$, showing that $F_{\text{left}}/F_{\text{right}} = 1{:}3.49$. In contrast, the Purcell factors of PC structures without SRR are $F_{\text{tot0}} = 3.41$, $F_{\text{left0}} = 0.12$, $F_{\text{right0}} = 0.51$, and $F_{\text{sc0}} = 2.78$, leading to $F_{\text{left0}}/F_{\text{right0}} = 1{:}4.17$. Note that $F_{\text{abs0}} = 0$ due to no metal SRR. It is obvious that the magnetic Purcell factor of $\sim 10^0$ is three orders of magnitude smaller than the electric Purcell factor because the radiation term for the magnetic dipole usually has the same magnitude as the electric quadrupole, which is much weaker than an electric dipole. The effective chiral magnetic Purcell factor $F_{\text{ev}} = F_{\text{left}} + F_{\text{right}}$ is only 7.89% and 4.40% for the split's $+x$ and $-x$ direction, respectively, because the scattering and metallic absorption waste most of the photonic energy. Though the spilt's direction cannot change the chirality, it helps enhance the effective spontaneous emission F_{ev} by a range of 79%, and chirality $F_{\text{left}}/F_{\text{right}}$ by a range of nearly 17%, when matching the chiral propagation.

Then, we change the position of SRR containing emitter $(1, i, 0)$ to point L3, and the chiral propagation turns left with the split in the $+x$ and $-x$ directions [Figs. 6(e) and 6(f)], the same as those without SRR [Figs. 5(d) and 5(h)–(j)]. For the $+x$ split's direction, the Purcell factors $F_{\text{tot}} = 7.27$, $F_{\text{abs}} = 5.79$, $F_{\text{left}} = 0.12$, $F_{\text{right}} = 0.04$, and $F_{\text{sc}} = 1.31$, showing that $F_{\text{left}}/F_{\text{right}} = 2.77{:}1$, leads to the chiral left photonic propagation [Fig. 6(e)]. For the $-x$ split's direction, the Purcell factors are $F_{\text{tot}} = 7.49$, $F_{\text{abs}} = 5.80$, $F_{\text{left}} = 0.18$, $F_{\text{right}} = 0.05$, and $F_{\text{sc}} = 1.46$, with the chirality $F_{\text{left}}/F_{\text{right}} = 3.67{:}1$. In contrast, the Purcell factors of PC structures without SRR are $F_{\text{tot0}} = 2.04$, $F_{\text{left0}} = 0.18$, $F_{\text{right0}} = 0.05$, and $F_{\text{sc0}} = 1.81$, leading to $F_{\text{left0}}/F_{\text{right0}} = 3.57{:}1$. Here, the effective chiral magnetic Purcell factor $F_{\text{ev}} = F_{\text{left}} + F_{\text{right}}$ is only 2.25% and 3.03% for the split's $+x$ and $-x$ direction, respectively, which is even smaller than the results of point M3, due to the longer distance from point L3 to the interface. Also, it is the emitter's position caused by magnetic helicity σ, not the split's direction, that changes the chirality, but the split's direction helps enhance F_{ev} and $F_{\text{left}}/F_{\text{right}}$ by a range of nearly 35% and 32%, respectively, when matching the chiral propagation.

Changing the spin of the emitter can also directly affect the chiral direction excited by SRR. As shown in Figs. 6(g) and 6(h), the emitter $(1, -i, 0)$ at point M3 excites the left chiral light transport, opposite to those of $(1, i, 0)$ [Figs. 6(c) and 6(d)]. The results of Purcell factors for emitter $(1, -i, 0)$ are almost mirror symmetric to those of $(1, i, 0)$. For the split's $+x$ direction, we obtain that $F_{\text{tot}} = 8.35$, $F_{\text{abs}} = 5.73$, $F_{\text{left}} = 0.28$, $F_{\text{right}} = 0.08$, and $F_{\text{sc}} = 2.25$, with the chirality $F_{\text{left}}/F_{\text{right}} = 3.42{:}1$. For the split's $-x$ direction, $F_{\text{tot}} = 8.77$, $F_{\text{abs}} = 5.88$, $F_{\text{left}} = 0.54$, $F_{\text{right}} = 0.13$, and $F_{\text{sc}} = 2.21$, with the chirality $F_{\text{left}}/F_{\text{right}} = 4.06{:}1$. In contrast, the Purcell factors of PC structures without SRR are $F_{\text{tot0}} = 3.39$, $F_{\text{left0}} = 0.51$, $F_{\text{right0}} = 0.12$, and $F_{\text{sc0}} = 2.75$, leading to $F_{\text{left0}}/F_{\text{right0}} = 4.10{:}1$.

Therefore, the silver SRR with magnetic response can perfectly work as a chiral emitter, providing a method of tuning the chiral direction of spontaneous emission enhancement by controlling the emitter's positions and polarizations and the split's directions. The emitter's positions, determined by magnetic helicity and its polarizations, can directly decide the chiral photonic propagation when fixing the finite size

of photonic structure to avoid chiral oscillation. The split's directions cannot change the chirality but help enhance the effective spontaneous emission and chirality. However, because of the significant metallic absorption and radiative scattering, the effective Purcell factor is not satisfactory, which means it may not be a good choice if one prioritizes the efficiency of photon utilization.

Finally, we briefly address the possibility of the experimental realization of our proposal. The 3D honeycomb topological PC slab structure can be fabricated with the existing processing micro- and nanotechnologies. The topological system works in the wavelength range between 1400 and 1620 nm, corresponding with optical communication bands. As the relative permittivity of the materials is set at 12 and 2, respectively, the structure can be fabricated in silicon and silicon dioxide. The lattice constant $a_0 = 740$ nm, cylinder diameter $d = 164$ nm, and cylinder height $h = 650$ nm in silicon can be realized with normal nanofabrication techniques such as EBL and ICP etching [37–39]. To realize the top-down inverse symmetry, the PC structure can be fabricated on a standard SOI chip. Then, the silicon PC structure can be covered with a silicon dioxide layer by spin-coating of polymer hydrogen silsesquioxane (HSQ) or direct silicon dioxide deposition [35,36,64,65]. The possible difficulty may be realizing the silver SRR as an emitter, because depositing metal nanostructures into PCs is challenging. However, the proposal of silver SRR is worth trying because it only needs room temperature, which will be cheaper and more accessible than quantum dots requiring low temperature and strong magnetic field [13]. The excitement of SRR can be either endogenous (such as dyes) or exogenous (such as outer pump) for the 3D photonic chip. Overall, because of the total consideration of feasibility in the design processing, it is promising to realize our proposal of the direction-tunable chiral spontaneous emission based on the topological honeycomb PC slab experimentally. Varieties of designs can be derived from our structures, such as air-hole photonic crystals.

VII. CONCLUSION

In conclusion, we propose direction-tunable chiral spontaneous emission based on magnetic helicity and finite-size effect in a topological honeycomb PC slab. We reveal the principle of chiral directions tuned by the emitter's position upon the magnetic helicity distribution of TM modes as a new real-space judgment of chiral directions. More importantly, we found a phenomenon of chirality oscillation caused by the finite size of honeycomb topological PCs in the frequency range of edge state channels, which also decides the photonic chiral propagation. This method of controlling 2D chiral modes can be extended to the 3D topological honeycomb PC slab with SiO_2-PC-SiO_2 sandwich structures containing a silver SRR as the emitter. By careful design, the 3D slab structure is convenient for fabricating the present manufacturing of on-chip photonic integration. Also, the SRR makes the entire system work at room temperature without a strong magnetic field. Our research reduces the threshold of on-chip chiral photonic application under topological protection, which is helpful for single-photon sources, photonic integrated chip manufacturing, and quantum information processing.

ACKNOWLEDGMENTS

We thank Ying Gu, Lingxiao Shan, Bowen Dong, and Fan Zhang for the helpful discussions. This work was supported by the National Key Research and Development Program of China (Grant No. 2022YFA1404804) and the National Natural Science Foundation of China (Grants No. 62325501 and No. 62135001).

APPENDIX A: A SIMPLIFIED ANALYTIC FRAMEWORK OF FINITE-SIZE HONEYCOMB TOPOLOGICAL PC STRUCTURE

For the E_z components of TM modes inside the honeycomb topological PC structure with finite size in the x direction, we have

$$E_z = \sum_m E_{z,m} e^{-im\beta_0 x} e^{-iq_x x}. \tag{A1}$$

Here, m is an arbitrary integer, $\beta_0 = 2\pi/a_0$ represents the Bloch wave vector, and q_x means the wave vector of edge state modes in the x direction. According to the finite-size coupled-wave theory [38,45], E_z can be described by the basic waves R and S as

$$E_z = (Re^{-i\beta_0 x} + Se^{i\beta_0 x})e^{-iq_x x}. \tag{A2}$$

The boundary conditions for the finite-size PC are

$$S|_{L/2} = rR|_{L/2}, \quad R|_{-L/2} = r'S|_{-L/2}. \tag{A3}$$

Here, L represents the PC length in the x direction, and r and r' represent the effective reflectivity. Boundaries could mix the edge state modes with wave vectors q_x and $-q_x$, i.e.,

$$\begin{bmatrix} R \\ S \end{bmatrix} = C_1 \begin{bmatrix} V_{11} \\ V_{21} \end{bmatrix} e^{-iq_x x} + C_2 \begin{bmatrix} V_{12} \\ V_{22} \end{bmatrix} e^{iq_x x}. \tag{A4}$$

Here, C_1, C_2 represent the overlapping coefficients, and $V_{ij}(i, i = 1, 2)$ represents the element of the basis vector. Combining Eq. (A3) with Eq. (A4), we have

$$\begin{vmatrix} (V_{21} - rV_{11})e^{-iq_x L/2} & (V_{22} - rV_{12})e^{iq_x L/2} \\ (V_{11} - r'V_{21})e^{iq_x L/2} & (V_{12} - r'V_{22})e^{-iq_x L/2} \end{vmatrix} = 0. \tag{A5}$$

Then, we obtain the edge state mode wave vector inside the finite-size PC as

$$q_x = \frac{1}{2iL} \ln \left[\frac{(V_{21} - rV_{11})(V_{12} - r'V_{22})}{(V_{11} - r'V_{21})(V_{22} - rV_{12})} \right] + \frac{n\pi}{L}. \tag{A6}$$

n should be the integer. Then, we have

$$\begin{aligned} C_2 &= -\frac{V_{21} - rV_{11}}{V_{22} - rV_{12}} e^{-iq_x L} C_1, \\ &= (-1)^{n+1} \sqrt{\frac{(V_{21} - rV_{11})(V_{11} - r'V_{21})}{(V_{22} - rV_{12})(V_{12} - r'V_{22})}} C_1. \end{aligned} \tag{A7}$$

It is easy to prove that $V_{11} = V_{22}, V_{21} = V_{12}$, and if $r = r'$, we have $C_2 = (-1)^{n+1} C_1$. For $C_2 = C_1$, we have

$$\begin{aligned} E_z &= \mathrm{R}e^{-i\beta_0 x} + \mathrm{S}e^{i\beta_0 x} \\ &= (V_{11}e^{-iq_x x} + V_{12}e^{iq_x x})e^{-i\beta_0 x} \\ &\quad + (V_{21}e^{-iq_x x} + V_{22}e^{iq_x x})e^{i\beta_0 x}. \end{aligned} \tag{A8}$$

It is easy to prove that

$$\begin{aligned} E_z(-x) &= (V_{11}e^{iq_x x} + V_{12}e^{-iq_x x})e^{i\beta_0 x} \\ &\quad + (V_{21}e^{iq_x x} + V_{22}e^{-iq_x x})e^{-i\beta_0 x} \\ &= E_z(x). \end{aligned} \tag{A9}$$

For $C_2 = -C_1$, we can get $E_z(-x) = -E_z(x)$ in the same way. Therefore, if n is even, $C_2 = -C_1$, and E_z is an odd mode in the x direction, while if n is odd, $C_2 = C_1$, and E_z is an even mode in the x direction. This characteristic of eigenmode parity leads to the chirality oscillation in the main text.

APPENDIX B: CHIRALITY OSCILLATION UNDER MATERIAL LOSS

One may be concerned about the impact of material loss on chiral propagation. Here, we give an imaginary part for ε_a and ε_d ranging from $0i$ to $0.05i$ in the 2D cases. The results are in Fig. 7. The loss nearly does not affect the eigenfrequencies, so we can still see the curves of chirality oscillation with a reduced amplitude; a larger loss leads to a smaller amplitude. If the loss is too large, such as the imaginary part over $0.05i$, the PC cannot support light transport, and the amplitude of C_{ln} tends to zero gradually, meaning no chiral propagation. Therefore, chirality oscillation still happens in moderate lossy systems with finite size.

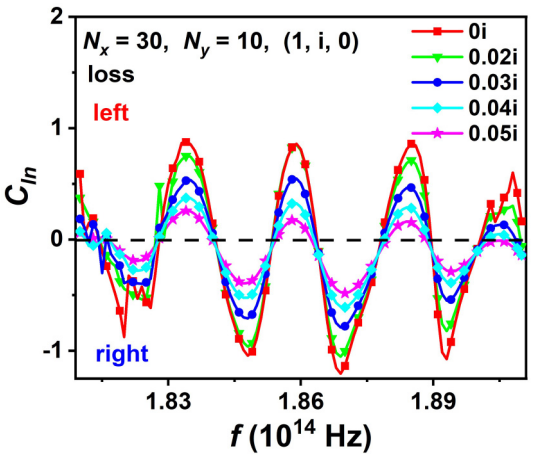

FIG. 7. Chirality oscillation considering material loss with finite size $N_x = 30, N_y = 10$. The chiral emitter takes $(1, i, 0)$ at the L3 point.

[1] Z. Wang, Y. Chong, J. D. Joannopoulos, and M. Soljačić, Observation of unidirectional backscattering-immune topological electromagnetic states, Nature (London) **461**, 772 (2009).

[2] Y. Poo, R.-x. Wu, Z. Lin, Y. Yang, and C. T. Chan, Experimental realization of self-guiding unidirectional electromagnetic edge states, Phys. Rev. Lett. **106**, 093903 (2011).

[3] S. A. Skirlo, L. Lu, Y. Igarashi, Q. Yan, J. Joannopoulos, and M. Soljačić, Experimental observation of large Chern numbers in photonic crystals, Phys. Rev. Lett. **115**, 253901 (2015).

[4] S. Mittal, E. A. Goldschmidt, and M. Hafezi, A topological source of quantum light, Nature (London) **561**, 502 (2018).

[5] M. Hafezi, E. A. Demler, M. D. Lukin, and J. M. Taylor, Robust optical delay lines with topological protection, Nat. Phys. **7**, 907 (2011).

[6] M. Hafezi, S. Mittal, J. Fan, A. Migdall, and J. Taylor, Imaging topological edge states in silicon photonics, Nat. Photon. **7**, 1001 (2013).

[7] X.-T. He, E.-T. Liang, J.-J. Yuan, H.-Y. Qiu, X.-D. Chen, F.-L. Zhao, and J.-W. Dong, A silicon-on-insulator slab for topological valley transport, Nat. Commun. **10**, 872 (2019).

[8] J. Noh, S. Huang, K. P. Chen, and M. C. Rechtsman, Observation of photonic topological valley Hall edge states, Phys. Rev. Lett. **120**, 063902 (2018).

[9] X. Cheng, C. Jouvaud, X. Ni, S. H. Mousavi, A. Z. Genack, and A. B. Khanikaev, Robust reconfigurable electromagnetic pathways within a photonic topological insulator, Nat. Mater. **15**, 542 (2016).

[10] T. Ma and G. Shvets, All-Si valley-Hall photonic topological insulator, New J. Phys. **18**, 025012 (2016).

[11] L.-H. Wu and X. Hu, Scheme for achieving a topological photonic crystal by using dielectric material, Phys. Rev. Lett. **114**, 223901 (2015).

[12] Y. Yang, Y. F. Xu, T. Xu, H.-X. Wang, J.-H. Jiang, X. Hu, and Z. H. Hang, Visualization of a unidirectional electromagnetic waveguide using topological photonic crystals made of dielectric materials, Phys. Rev. Lett. **120**, 217401 (2018).

[13] S. Barik, A. Karasahin, C. Flower, T. Cai, H. Miyake, W. DeGottardi, M. Hafezi, and E. Waks, A topological quantum optics interface, Science **359**, 666 (2018).

[14] S. Yves, R. Fleury, T. Berthelot, M. Fink, F. Lemoult, and G. Lerosey, Crystalline metamaterials for topological properties at subwavelength scales, Nat. Commun. **8**, 16023 (2017).

[15] Y. V. Kartashov and D. V. Skryabin, Bistable topological insulator with exciton-polaritons, Phys. Rev. Lett. **119**, 253904 (2017).

[16] P. D. Anderson and G. Subramania, Unidirectional edge states in topological honeycomb-lattice membrane photonic crystals, Opt. Express **25**, 23293 (2017).

[17] S. Barik, H. Miyake, W. DeGottardi, E. Waks, and M. Hafezi, Two-dimensionally confined topological edge states in photonic crystals, New J. Phys. **18**, 113013 (2016).

[18] B.-Z. Xia, T.-T. Liu, G.-L. Huang, H.-Q. Dai, J.-R. Jiao, X.-G. Zang, D.-J. Yu, S.-J. Zheng, and J. Liu, Topological phononic insulator with robust pseudospin-dependent transport, Phys. Rev. B **96**, 094106 (2017).

[19] M. C. Rechtsman, J. M. Zeuner, Y. Plotnik, Y. Lumer, D. Podolsky, F. Dreisow, S. Nolte, M. Segev, and A. Szameit, Photonic Floquet topological insulators, Nature (London) **496**, 196 (2013).

[20] S. Arora, T. Bauer, N. Parappurath, R. Barczyk, E. Verhagen, and L. Kuipers, Breakdown of spin-to-helicity locking at the nanoscale in topological photonic crystal edge states, Phys. Rev. Lett. **128**, 203903 (2022).

[21] L. Lu, J. D. Joannopoulos, and M. Soljačić, Topological photonics, Nat. Photon. **8**, 821 (2014).

[22] A. B. Khanikaev and G. Shvets, Two-dimensional topological photonics, Nat. Photon. **11**, 763 (2017).

[23] L. Lu, J. D. Joannopoulos, and M. Soljačić, Topological states in photonic systems, Nat. Phys. **12**, 626 (2016).

[24] T. Ozawa, H. M. Price, A. Amo, N. Goldman, M. Hafezi, L. Lu, M. C. Rechtsman, D. Schuster, J. Simon, O. Zilberberg, and I. Carusotto, Topological photonics, Rev. Mod. Phys. **91**, 015006 (2019).

[25] S. Mittal, S. Ganeshan, J. Fan, A. Vaezi, and M. Hafezi, Measurement of topological invariants in a 2D photonic system, Nat. Photon. **10**, 180 (2016).

[26] M. Xiao, Z. Q. Zhang, and C. T. Chan, Surface impedance and bulk band geometric phases in one-dimensional systems, Phys. Rev. X **4**, 021017 (2014).

[27] J. Noh, W. A. Benalcazar, S. Huang, M. J. Collins, K. P. Chen, T. L. Hughes, and M. C. Rechtsman, Topological protection of photonic mid-gap defect modes, Nat. Photon. **12**, 408 (2018).

[28] A. Amo, When quantum optics meets topology, Science **359**, 638 (2018).

[29] Z. Qian, Z. Li, H. Hao, L. Shan, Q. Zhang, J. Dong, Q. Gong, and Y. Gu, Absorption reduction of large Purcell enhancement enabled by topological state-led mode coupling, Phys. Rev. Lett. **126**, 023901 (2021).

[30] T. Dai *et al.*, Topologically protected quantum entanglement emitters, Nat. Photon. **16**, 248 (2022).

[31] W. Liu, Z. Ji, Y. Wang, G. Modi, M. Hwang, B. Zheng, V. J. Sorger, A. Pan, and R. Agarwal, Generation of helical topological exciton-polaritons, Science **370**, 600 (2020).

[32] A. Blanco-Redondo, B. Bell, D. Oren, B. J. Eggleton, and M. Segev, Topological protection of biphoton states, Science **362**, 568 (2018).

[33] X.-D. Chen, W.-M. Deng, F.-L. Shi, F.-L. Zhao, M. Chen, and J.-W. Dong, Direct observation of corner states in second-order topological photonic crystal slabs, Phys. Rev. Lett. **122**, 233902 (2019).

[34] F. Gao *et al.*, Probing topological protection using a designer surface plasmon structure, Nat. Commun. **7**, 11619 (2016).

[35] S. J. Khatib and S. T. Oyama, Silica membranes for hydrogen separation prepared by chemical vapor deposition (CVD), Sep. Purif. Technol. **111**, 20 (2013).

[36] J. Farkas, M. J. Hampden-Smith, and T. T. Kodas, FTIR studies of the adsorption/desorption behavior of copper chemical vapor deposition precursors on silica. 1. Bis(1,1,1,5,5,5-hexafluoroacetylacetonato)copper(II), J. Phys. Chem. **98**, 6753 (1994).

[37] K. Hirose, Y. Liang, Y. Kurosaka, A. Watanabe, T. Sugiyama, and S. Noda, Watt-class high-power, high-beam-quality photonic-crystal lasers, Nat. Photon. **8**, 406 (2014).

[38] Z. Chen, X. Yin, J. Jin, Z. Zheng, Z. Zhang, F. Wang, L. He, B. Zhen, and C. Peng, Observation of miniaturized bound states in the continuum with ultra-high quality factors, Sci. Bull. **67**, 359 (2022).

[39] Y. Ren, P. Li, Z. Liu, Z. Chen, Y.-L. Chen, C. Peng, and J. Liu, Low-threshold nanolasers based on miniaturized bound states in the continuum, Sci. Adv. **8**, eade8817 (2022).

[40] F. Zhang, J. Ren, L. Shan, X. Duan, Y. Li, T. Zhang, Q. Gong, and Y. Gu, Chiral cavity quantum electrodynamics with coupled nanophotonic structures, Phys. Rev. A **100**, 053841 (2019).

[41] D. O'Connor, P. Ginzburg, F. J. Rodríguez-Fortuño, G. A. Wurtz, and A. V. Zayats, Spin–orbit coupling in surface plasmon scattering by nanostructures, Nat. Commun. **5**, 5327 (2014).

[42] Z. Qian, J. Ren, F. Zhang, X. Duan, Q. Gong, and Y. Gu, Nanoscale quantum plasmon sensing based on strong photon-exciton coupling, Nanotechnology **31**, 125001 (2020).

[43] J. Ren, Y. Gu, D. Zhao, F. Zhang, T. Zhang, and Q. Gong, Evanescent-vacuum-enhanced photon-exciton coupling and fluorescence collection, Phys. Rev. Lett. **118**, 073604 (2017).

[44] Z. Qian, Y. Chen, and C. Peng, Topologically protected strong photon-exciton coupling, Phys. Rev. A **108**, 043706 (2023).

[45] Z. Chen, X. Yin, P. Li, Z. Zheng, Z. Zhang, F. Wang, and C. Peng, Analytical theory of finite-size photonic crystal slabs near the band edge, Opt. Express **30**, 14033 (2022).

[46] J. K. Asbóth, L. Oroszlány, and A. Pályi, A short course on topological insulators, in *Band Structure and Edge States in One and Two Dimensions*, Lecture Notes in Physics Vol. 919 (Springer, Cham, 2016).

[47] Y. Liang, C. Peng, K. Sakai, S. Iwahashi, and S. Noda, Three-dimensional coupled-wave analysis for square-lattice photonic crystal surface emitting lasers with transverse-electric polarization: Finite-size effects, Opt. Express **20**, 15945 (2012).

[48] C. Peng, Y. Liang, K. Sakai, S. Iwahashi, and S. Noda, Three-dimensional coupled-wave theory analysis of a centered-rectangular lattice photonic crystal laser with a transverse-electric-like mode, Phys. Rev. B **86**, 035108 (2012).

[49] Y. Liang, C. Peng, K. Ishizaki, S. Iwahashi, K. Sakai, Y. Tanaka, K. Kitamura, and S. Noda, Three-dimensional coupled-wave analysis for triangular-lattice photonic-crystal surface-emitting lasers with transverse-electric polarization, Opt. Express **21**, 565 (2013).

[50] Y. Yang, C. Peng, Y. Liang, Z. Li, and S. Noda, Three-dimensional coupled-wave theory for the guided mode resonance in photonic crystal slabs: TM-like polarization, Opt. Lett. **39**, 4498 (2014).

[51] Y. Yang, C. Peng, Y. Liang, Z. Li, and S. Noda, Analytical perspective for bound states in the continuum in photonic crystal slabs, Phys. Rev. Lett. **113**, 037401 (2014).

[52] L. Ni, Z. Wang, C. Peng, and Z. Li, Tunable optical bound states in the continuum beyond in-plane symmetry protection, Phys. Rev. B **94**, 245148 (2016).

[53] J. Breeze, K.-J. Tan, B. Richards, J. Sathian, M. Oxborrow, and N. M. Alford, Enhanced magnetic Purcell effect in room-temperature masers, Nat. Commun. **6**, 6215 (2015).

[54] S. Karaveli and R. Zia, Spectral tuning by selective enhancement of electric and magnetic dipole emission, Phys. Rev. Lett. **106**, 193004 (2011).

[55] A. P. Slobozhanyuk, A. N. Poddubny, A. E. Krasnok, and P. A. Belov, Magnetic Purcell factor in wire metamaterials, Appl. Phys. Lett. **104**, 161105 (2014).

[56] D. G. Baranov, R. S. Savelev, S. V. Li, A. E. Krasnok, and A. Alù, Modifying magnetic dipole spontaneous emission with nanophotonic structures, Laser Photon. Rev. **11**, 1600268 (2017).

[57] T. Feng, W. Zhang, Z. Liang, Y. Xu, and A. E. Miroshnichenko, Isotropic magnetic Purcell effect, ACS Photon. **5**, 678 (2018).

[58] L. Aigouy, A. Cazé, P. Gredin, M. Mortier, and R. Carminati, Mapping and quantifying electric and magnetic dipole luminescence at the nanoscale, Phys. Rev. Lett. **113**, 076101 (2014).
[59] D. R. Smith, J. B. Pendry, and M. C. K. Wiltshire, Metamaterials and negative refractive index, Science **305**, 788 (2004).
[60] R. A. Shelby, D. R. Smith, and S. Schultz, Experimental verification of a negative index of refraction, Science **292**, 77 (2001).
[61] J. Pendry, A. Holden, D. Robbins, and W. Stewart, Magnetism from conductors and enhanced nonlinear phenomena, IEEE Trans. Microwave Theory Tech. **47**, 2075 (1999).
[62] P. B. Johnson and R. W. Christy, Optical constants of the noble metals, Phys. Rev. B **6**, 4370 (1972).
[63] M. S. Tame, K. McEnery, Ş. Özdemir, J. Lee, S. A. Maier, and M. Kim, Quantum plasmonics, Nat. Phys. **9**, 329 (2013).
[64] L. T. Varghese, L. Fan, J. Wang, Y. Xuan, and M. Qi, Rapid and low-cost prototyping of 3D nanostructures with multi-layer hydrogen silsesquioxane scaffolds, Small **9**, 4237 (2013).
[65] S. Lis, R. Dylewicz, J. Mysliwiec, A. Miniewicz, and S. Patela, Application of flowable oxides in photonics, Mater. Sci.-Poland **26**, 189 (2008).